Lithium Trapping in Alloy forming Electrodes and Current Collectors for Lithium based Batteries

David Rehnlund[1]*, Fredrik Lindgren[1], Solveig Böhme[1], Tim Nordh[1], Yiming Zou[1], Jean Pettersson[2], Ulf Bexell[3], Mats Boman[1], Kristina Edström[1], Leif Nyholm[1]*

*Corresponding authors. E-mail: David.Rehnlund@kemi.uu.se, Leif.Nyholm@kemi.uu.se

This PDF file includes:

Materials and methods

Supplementary text

Figs S1 to S13

Tables S1 to S2

References

1. Materials and methods

Manufacturing of the Sn and Si electrodes

The tin were manufactured with a template-assisted electrodeposition approach [1, 2] in which a porous membrane with a nominal pore size of 200 nm (Cyclopore for Sn and Anodisc for Cu, Whatman) was wetted with electrolyte solution and placed on top of a copper substrate. The latter had been cleaned with ethanol (Solveco, 99.5 %) for 10 minutes in an ultrasonic bath. A piece of an electrolyte soaked glass fibre membrane (0.26 mm thick, Whatman) was placed on top of the polymer membrane and the Pt foil counter electrode was then placed on top of the stack. The assembly was finally placed in an electrochemical cell filled with 20 ml electrolyte. The tin nanorod deposition was carried out in an aqueous solution of 0.2 M tin(II) chloride (Sigma Aldrich, > 98 %) and 0.4 M trisodium citrate (Sigma Aldrich > 99 %) with a pH of 4.

The nanorod electrodeposition was carried out with a Versastat 4 Potentiostat (Princeton Applied Research) and the deposition process comprised an initial 0.5 s long (nucleation) potential step to -1.2 V followed by a repeated galvanostatic pulse scheme composed of a 1 ms long pulse with a current density of -30 mA cm^{-2} and a 9 ms long pulse with a current density of 0 mA cm^{-2}. The latter galvanostatic scheme was repeated 60000 times, which gave rise to a total deposition time of about 10 minutes. The membrane was then dissolved in dichloromethane (Sigma Aldrich) to expose the freestanding tin nanorods.

The silicon composite electrodes were prepared using 80% of crystalline silicon powder (~50 nm, Alfa Aesar), 12% conductive carbon black (SuperP, Erachem Comilog) and 8% sodium carboxymethyl cellulose (CMC, M_w = 700.000, DS = 0.9, Sigma Aldrich) binder. A slurry based on a water−ethanol solution (70%/30% v/v) was mixed in a Retsch planetary mill for 60 min and was then cast on either 20 μm thick copper or 15 μm thick nickel current collectors. The electrodes were then dried at 60 °C for 12 h to yield a final coating thickness of about 15 μm. Circular electrodes (with a diameter of 13 mm) were then punched out and dried for 8 h at 120 °C in a vacuum oven inside an argon filled glovebox. The electrochemical cells were subsequently assembled by stacking the Si/C/CMC composite electrode, a polymer based separator soaked with the electrolyte (1 M LiPF$_6$ dissolved in EC:DEC 1:1 wt.%) and a piece of lithium foil. This stack was finally sealed into a polymer coated aluminium pouch inside an argon filled glovebox.

Fabrication of boron-doped diamond films and lithium coated boron-doped diamond films

Boron-doped diamond films were deposited on silicon (100) wafers using a loadlock hot filament chemical vapour deposition reactor (model BWI 1000 HFCVD, Blue Wave Semiconductors, Inc.). Prior to the diamond deposition, the silicon wafers were seeded with 4-5 nm large nanodiamond crystallites using a ≪0.5% aqueous solution (New Metals & Chemicals Corporation) by ultrasonic treatment for 60 min, after which the surface was cleaned with ethanol. Three carburized tungsten filaments situated 5 mm from the substrate were heated to

2200 °C during the diamond growth while the substrate temperature was set to 700 °C. A gas mixture containing 99 standard cubic centimetre (sccm) of hydrogen and 1 sccm of methane was employed and kept at a constant pressure of 5 Torr. The deposition was carried out with continuous rotation of the silicon substrate during the four-hour deposition in which 0.01 sccm of gaseous trimethylborane $(B(OCH_3)_3)$ was used as a boron dopant precursor.

Lithium coated boron-doped diamond films were prepared via lithium deposition in a polymer covered aluminium pouch cell in which a boron-doped diamond film and a Li foil were separated by a porous polymer membrane (Solupor) soaked in 1 M $LiPF_6$ dissolved in a 1:1 wt.% EC:DEC mixture. The lithium plating was performed with a constant current density of 100 µA/cm^2 and a fixed lithium deposition charge of 1.0 mAh.

Characterization of the boron-doped diamond films

The Raman experiments were carried out at room temperature using an inVia Raman Microscope (Renishaw) with a wavelength of 532 nm. The boron doping level was estimated using the Mott-Schottky plot method employing an Electrochemical Workstation (CH Instruments) and an aqueous 0.5 M NaCl solution at room temperature. A three-electrode setup comprising a boron-doped diamond working electrode, a platinum counter electrode and a Ag/AgCl reference electrode was employed.

Elemental analyses of electrode materials and current collectors

The tin electrodes as well as the nickel, copper and titanium samples were digested in 5.0 ml sub-boiled HNO_3 (14 M) in 50 ml PTFE centrifuge tubes. The heat was increased stepwise from room temperature to the boiling point of the nitric acid (135°C) and kept there for three hours. After the digestion the sample was quantitatively transferred to a Falcon tube and diluted to 50 ml with MQ-filtered ultrapure water.

The boron-doped diamond films exposed to lithium for up to seven days were analysed as follows. The lithium metal foil was first removed from the sample surface and the sample was quickly cleaned with water to remove any residual lithium. The samples were then digested until dryness in a mixture of 3.0 ml sub-boiled HNO_3 (14 M) and 1.0 ml HF (48% pro analysis) at 100 °C overnight in PFA centrifuge tubes using a temperature controlled aluminium block. This digestion was subsequently repeated three times, first with 2.0 ml HF, then with a mixture of 3.0 ml HNO_3 and 1.0 ml HF and finally with a mixture of 2.0 ml HF and 2.0 ml H_2O_2. After adding 3.0 ml HNO_3 and 3.0 ml MQ-filtered ultrapure water, the solution was heated to the boiling point and was then allowed to cool down. The resulting solution was quantitatively transferred to 15 ml centrifuge tubes (i.e., Falcon™ tubes) and diluted to 10.0 ml with MQ-filtered ultrapure water. Although a complete dissolution of the boron-doped samples could not be obtained, it is still reasonable to assume that the lithium was quantitatively extracted from the samples.

The lithium contents in the different solutions were determined with a Spectro Cirros CCD ICP-AES instrument (Kleve, Germany) using the settings recommended by the manufacturer (Li 670.780 nm) and matrix matched lithium calibration standards. The samples were aspirated 45 seconds before triplicate readings during 24 seconds were made and the reported values are averages of these three determinations.

The amounts of lithium present in the silicon composite electrodes after the lithium depositions were determined as follows. The electrodes were first washed three times in dimethyl carbonate (DMC) to remove traces of the electrolyte. The electrodes were then carefully exposed to water to extract most of the lithium. This gave rise to a vivid reaction (i.e. $2 Li + 2 H_2O = 2 Li^+ + 2 OH^- + H_2$) and the formation of a brownish gel-like precipitate, most likely containing the silicon particles and the other components of the composite electrode. The copper current collectors were removed, rinsed with MQ-filtered ultrapure water and subsequently dissolved in HNO_3 after which the amounts of lithium in the solutions were determined as described above. The solutions containing the precipitates were treated with 10% HNO_3 and centrifuged and the amounts of lithium in the supernatants were determined. These solutions were found to contain about 96% of the total amount of lithium found in the analyses. The precipitate was first digested until dryness three times using a mixture of 3.0 ml of HNO_3 and 1.0 ml HF. Since this did not result in a complete dissolution of the precipitate, the lithium determination was carried out by introducing the slurry, most likely containing graphite particles, directly into the ICP-AES instrument. As the graphite particles were completely atomized in the plasma, the amount of lithium in the precipitate could still be determined.

TOF-SIMS analyses of boron-doped diamond films

The time-of-flight secondary ion mass spectrometry (TOF-SIMS) analyses were performed using a PHI TRIFT II instrument with a pulsed liquid metal ion gun equipped with a primary ion source enriched in ^{69}Ga isotopes. Depth profiles were obtained by sputtering a surface area of 75x75 μm with a continuous non-pulsed beam with primary ion energy of 15 keV and an aperture giving a current of approximately 2 nA. Positive static SIMS mode was used to analyse an area of 50x50 μm in the centre of the sputtered area. All SIMS spectra were calibrated using peaks with known mass/charge ratio, such as lithium ($^7Li^+$), carbon ($^{12}C^+$) and the Ga primary ion ($^{69}Ga^+$).

HAXPES analyses of boron-doped diamond films

The hard X-ray photoelectron spectroscopy (HAXPES) measurements were made at KMC-1 beamline, HIKE end-station at the BESSY synchrotron radiation source, Helmholtz Centrum Berlin using a Scienta R4000 analyser. The cells were opened in an argon filled glovebox ($[H_2O]$<5 ppm, $[O^2]$<1 ppm), washed with DMC and mounted onto a sample holder using copper tape. The samples were transferred from the glovebox to the analysis chamber using an airtight transfer rod to prevent air contamination. The core level of C1s was measured with 2005

and 6015 eV for the pristine and cycled electrodes. Energy calibration was made using the Au4f peak.

Electrochemical measurements

The voltammetric and chronopotentiometric measurements were carried out with a VMP2 (Bio-Logic) galvanostat/potentiostat using plastic pouch cells containing the different electrode materials, assembled under an argon atmosphere with $[O_2]$ and $[H_2O]$ levels below 1 ppm. Prior to the assembly all electrodes were dried under vacuum at 120 °C for five hours in a glovebox. The silicon composite electrode containing cells were assembled by stacking a Si/C/CMC composite electrodes, two 15 µm thick plastic membranes (Solupore) soaked with 50 µl of 1 M $LiPF_6$ in EC:DEC 1:1 and a lithium foil. The tin nanorod based cells were analogously designed except that glass fibre separators (0.26 mm thick, Whatman) were used instead of the Solupore separators. The lithium deposition on the boron-doped diamond electrodes was performed in a cell comprising the boron-doped diamond electrode and a Li foil separated by two 15 µm thick plastic membranes (Solupore) soaked with 50 µl of 1 M $LiPF_6$ in EC:DEC 1:1.

2. Influence of the cycling conditions and two-way diffusion on the shapes of the Sn capacity vs. cycle number plots

In Figure 1b in the main article it is seen that capacity versus cycle number plots with different shapes were obtained for the tin nanorod electrodes for cycling to 1.0 and 2.5 V vs. Li^+/Li, respectively. This indicates the presence of a potential and/or time effect. The presence of a native tin oxide film on the tin nanorods is very unlikely to have affected the shapes of the capacity versus cycle number plots significantly as the charges associated with such native oxide layers are very small in comparison with the charges due to the lithium alloy formation [3]. To study the phenomenon further, cyclic voltammograms were recorded between 0.1 and 1.0 V (at a rate of 1.0 mV/s) but with a 3000 s long pause at 1.0 V vs. Li^+/Li on each cycle. The resulting capacity versus cycle number plot is shown in Figure S1 which also features the cyclic voltammograms obtained for cycling between 0.1 and 1.0 V with and without the pause. As the pause corresponded to the time required to scan to 2.5 V and back to 1.0 V, the total time for each cycle should have been the same as for the scans to 2.5 V. Irrespective of the cycling conditions, an initial capacity increase followed by a capacity loss was seen although the loss was seen at different cycle numbers depending on how the cycling was performed. It is also seen that the capacities were significantly smaller for cycling up to 2.5 V than for scanning to 1.0 V and that this mainly was due to a large decrease taking place during the first few cycles. A faster capacity decrease was also seen in the presence of the pause during the scans to 1.0 V.

These results show that the capacities were affected by at least two phenomena and that their influence was different at different stages in the cycling. While increasing capacities during cycling are typically due to increases in the electroactive area of the electrode, decreasing capacities are generally seen for lithium alloy forming materials. The latter are typically ascribed

to a combination of SEI formation and volume expansion effects. Since the present experiments were carried out with a lithium counter electrode with a large capacity, SEI formation can, however, not explain the observed capacity decreases as is explained in the main article. It should also be noted that the influence of SEI effects should be most pronounced on the first cycles, i.e. in the region where the capacity increased rather than decreased. A loss of capacity due to a pulverization of the tin nanorods due to the volumetric expansion (e.g. 280 % for $Li_{3.75}Si$ [4]) is also unlikely as no signs of any such degradation of the nanorods were found when inspecting the electrodes after the experiments and as such effects likewise would be expected to be most pronounced in the beginning of the cycling. Note also that the volume expansion would be expected to take place only at potentials below 1.0 V vs. Li^+/Li and therefore cannot explain the difference seen when scanning to 1.0 and 2.5 V, nor the influence of the pause at 1.0 V.

The results indicate that the shape of the capacity versus cycle number plots depended on the time spent at potentials where the lithium in the alloy should undergo oxidation, i.e. at potentials where there was very little electrochemical activity. This behaviour can be explained based on the two-way diffusion model described in the main article as the lithium deposited during the reductive scan would have time to diffuse longer into the electrode during scans during scans to 2.5 V than when scanning only to 1.0 V (in the absence of a pause there). This also means that a larger fraction of the deposited lithium would be trapped after introducing the 3000 s long pause during the scans to 1.0 V. The different behaviour seen for the scans to 2.5 V and 1.0 V in the presence of the pause can then be explained by the fact that a significantly lower surface concentration of lithium should be obtained at 2.5 V. In Figure 1a it can be seen that there was still lithium oxidation at potentials higher than 1.0 V on the first scan most likely due to mass transport limitations. At 2.5 V the surface concentration of lithium should be practically zero and a thicker diffusion layer should also develop during the scans to 2.5 V than during the scans to 1.0 V. The latter most likely explains the significant capacity drop seen during the first few cycles for the scans to 2.5 V as the lithium trapping capacity of the electrode should be higher on the reductive scans after scanning to 2.5 V.

It can hence be concluded that a more pronounced lithium trapping effect was present when scanning to 2.5 V and with the pause during the scans to 1.0 V. In both cases, a lithium oxidation time which was longer than the lithium deposition time was obtained. This situation is therefore very similar to those in Figure 2b and c where a prolonged oxidation step was seen to give rise to a significant loss of capacity on the next cycle. This can be explained based on the thick lithium diffusion layer developed inside the electrode during the oxidation. On the subsequent deposition of lithium (taking place on a shorter time scale), the diffusion of lithium towards the internal parts of the electrode is hence more pronounced than when the oxidation step is of the same duration as the lithium deposition step. After a long oxidation step, the situation should therefore be similar to that on the first cycle when using a pristine electrode. The lithium trapping effect should consequently be particularly pronounced on the first cycle for a pristine electrode as the lithium concentration profile obtained after the second cycle would slow down the diffusion of lithium towards the internal parts of the electrode as is shown in Figure 3.
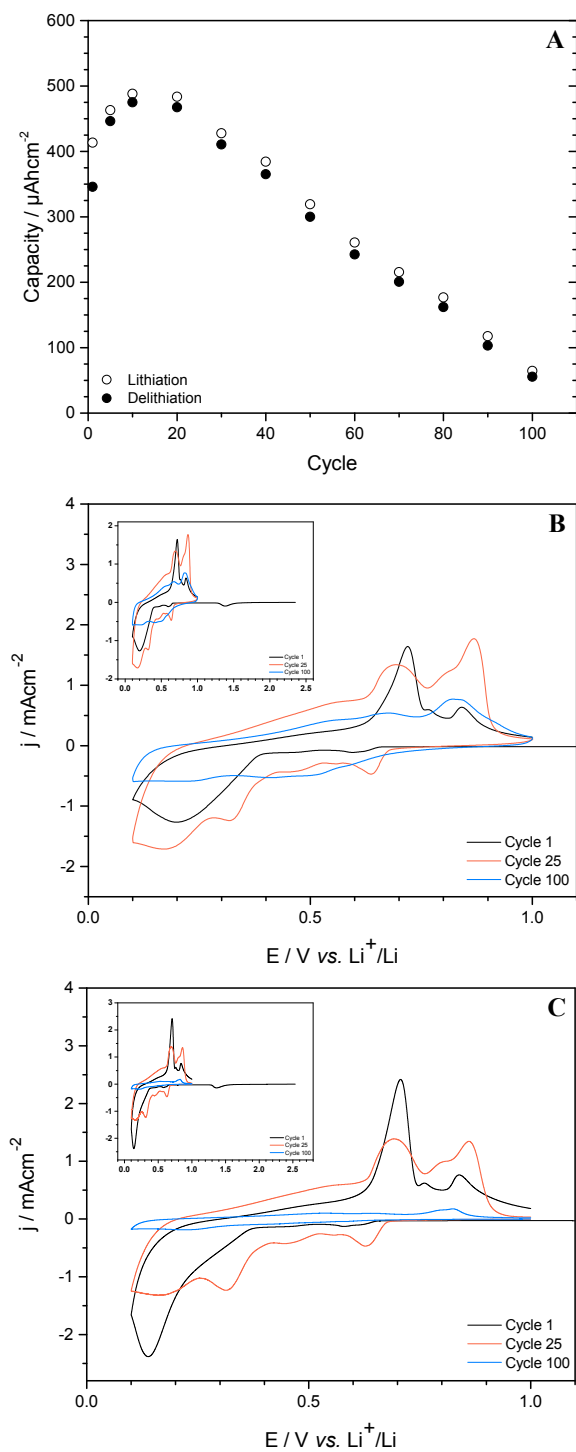
Fig. S1. Areal capacities and cyclic voltammograms obtained with Sn nanorod electrodes in Li-half cells. (**A**) Areal capacities and Q_{ox}/Q_{red} ratios as a function of the cycle number for cycling between 0.1 and 1.0 V vs. Li$^+$/Li in the presence of a 3000 s long pause at 1.0 V on each cycle. (**B**) Cyclic voltammograms, depicting the 1st, 25th and 100th cycles, recorded between 0.1 and 1.0 V vs. Li$^+$/Li. (**C**) Cyclic voltammograms, depicting the 1st, 25th and 100th cycles,

recorded between 0.1 and 1.0 V vs. Li$^+$/Li with a 3000 s long pause at 1.0 V on each cycle. The insets show the full voltammograms which were recorded in the cathodic direction from the open circuit potential, i.e. about 2.3 to 2.5 V vs. Li$^+$/Li. The scan rate was 1.0 mV/s in all cases.
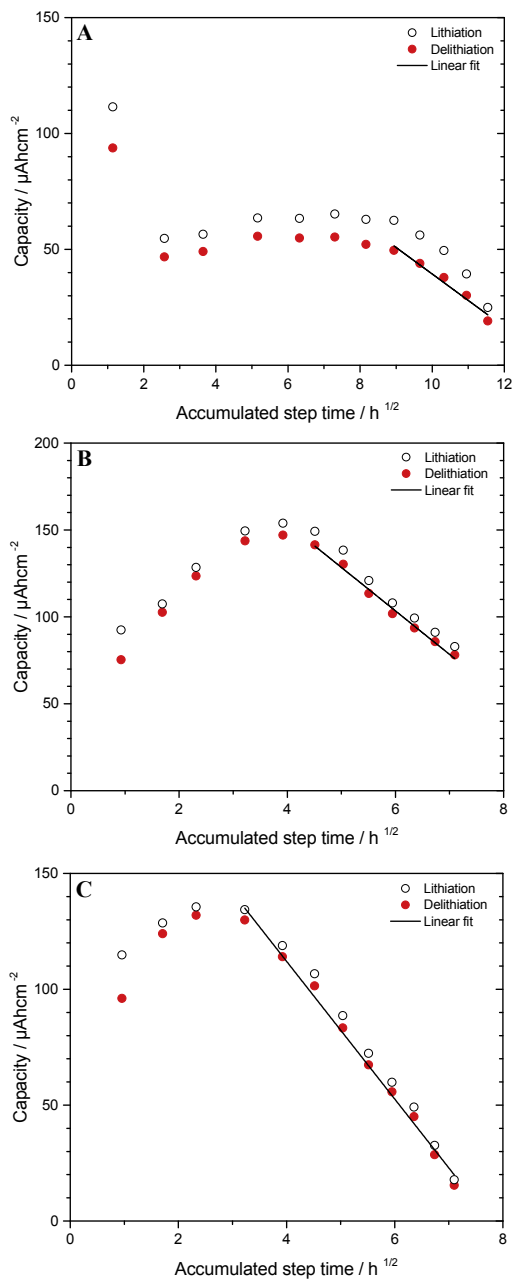
Fig. S2. Areal capacity versus square root of time plots for Sn nanorod electrodes. (A) The tin nanorod electrodes were cycled between 0.1 and 2.5 V, **(B)** 0.1 and 1.0 V and **(C)** 0.1 and 1.0 V with a 3000 s long pause 1.0 V on each scan, respectively, using a scan rate of 1.0 mV/s. The plots cover the regions in which the capacity decreased with increasing scan number, i.e. cycle 60 to 100 in (A), 40 to 100 in (B) and 20 to 100 in (C). The solid lines represent linear least squares fits to the delithiation (i.e. Li oxidation) data.

The initial increase in the capacity seen in Figure 1b and Fig S1 must, therefore, be due to another superimposed phenomenon, most likely the generation of a larger electrode surface area as a result of the amorphisation of the electrode. This hypothesis is supported by previous findings for aluminium electrodes[5-7]. Such amorphisation effects should be particularly pronounced during the initial part of the cycling and can also be expected to be more significant for cycling to 1.0 V than to 2.5 V as more time would be available for stress relaxation during the cycling in the latter case. The shapes of the capacity versus cycle number plots can therefore be explained by a combination of electrode surface area increases due to amorphisation of the electrodes [5-7] and capacity decreases caused by lithium trapping in the electrodes.

3. Li trapping and SEI formation with the Sn nanorod electrodes

As seen in Figure S3, the determinations of the lithium amounts in the cycled tin nanorod electrodes indicated that their lithium amount increased linearly with the cycle number and that about 1.27 μg lithium was trapped in the electrode on each cycle. The latter amount corresponds to a charge of 17.8 mC per cycle. As is shown in Table S1, the latter charge was compared with the difference between the reduction and oxidation charges for each cycle. It was then found that the trapped amount of lithium on average corresponded to about 50% of the difference between the reduction and oxidation charges. As this fraction was only about 28% on the first cycle, it is reasonable to assume that the remaining charge was due to SEI formation since most of the SEI layer should be formed on the first cycle. On the first cycle, the SEI charge of 46 mC would correspond to the formation of a SEI layer with a thickness of about 7 nm based on an electrode area of 23 cm^2 (typical for these nanorod electrodes) and an assumed two-electron SEI forming reaction yielding a species with an assumed molecular weight of 150 g/mol and an assumed density of 2 g/cm^3. Given these assumptions, an SEI layer with a thickness of about 3 nm should then have been formed on the subsequent cycles most likely due to a partial dissolution of the SEI layer. Such a dissolution rate, which would correspond to about 2 nm/hour, is in fact also supported by XPS results [8, 9]. A partial dissolution of the SEI [10] is further supported by the fact that the SEI thickness should have been about 290 nm after 100 cycles in the absence of any dissolution. This value is in contrast with the experimental findings [9-13] indicating the presence of a SEI layer with a thickness of less than 20 nm. The data in Table S1 therefore demonstrate that the differences between the reduction and oxidation charges were due to lithium trapping and SEI formation.

Since the SEI charge on the first cycle was about 46 mC it can also be calculated that an average SEI current of about 0.1 mA should have been present, assuming a scan rate of 1 mV/s and a SEI peak width of 400 mV. This indicates that the broad first cycle reduction peak at about 1.5 V seen in Figure 1a in the main article was due to a combination of SEI formation and reduction of the native SnO_2 layer to SnO. As discussed elsewhere [3, 14], the current due to the SEI formation is, however, difficult to detect in the presence of thicker SnO_2 films. Note that SEI formation at

potentials below about 1.5 V also would explain the reduction peak seen at about 1.4 V on the first oxidative scan in Figure 1a.
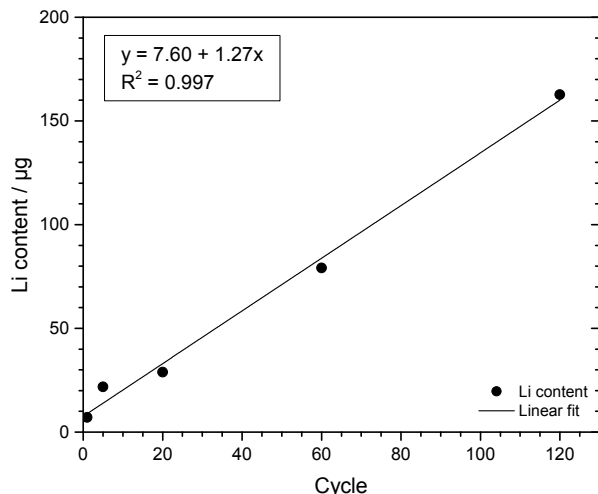
Fig. S3. Residual Li content in oxidised tin nanorod electrodes. The lithium amount in cycled tin nanorod electrodes, determined with ICP-AES, as a function of the cycle number. The electrodes were cycled between 0.1 and 2.5 V vs. Li^+/Li at a scan rate of 1.0 mV/s and the scans were terminated at 2.5 V vs. Li^+/Li. The solid line represents a linear least squares fit.

Table S1. Li deposition and estimated SEI charges for nanostructured tin electrodes.

Cycle	$Q_{red} - Q_{ox}$ (mC)	Li charge (%)	Q_{SEI} (mC)	SEI thickness (nm)	Maximum SEI thickness (nm)
1	64	28	46	7.2	9.9
5	29	61	11	1.7	4.5
10	27	67	9	1.4	4.1
20	28	62	11	1.7	4.4
30	31	58	13	2.0	4.7
40	36	50	18	2.8	5.6
50	39	46	21	3.2	6.0
60	47	38	29	4.5	7.2
70	44	40	26	4.1	6.9
80	42	43	24	3.7	6.5
90	33	53	16	2.4	5.2
100	21	85	3	0.5	3.3
Average	*37*	*53*	*19*	*2.9*	*5.7*
Sum				*290[a]*	*570[b]*

[a,b] Estimated SEI thickness after 100 cycles in the presence and absence of any lithium trapping, respectively. The SEI thickness estimations are based on an electrode area of 25 cm^2 assuming a two-electron SEI forming reaction yielding a product with a molar weight of 150 g/mol and a density of 2 g/cm^3.

4. Li trapping in Al nanorod electrodes

In Figure S4 it is seen that linear plots of the capacity versus the cycle number (and hence the square root of the time) likewise were obtained with published aluminium nanorod electrode cyclic voltammetric data [5]. These electrodes, which had a native layer of Al_2O_3, were cycled between 0.1 and 3 V vs. Li^+/Li at a scan rate of 1.0 mV/s. The plots were found to be linear during the first 20 cycles, after which the capacity dropped to close to zero. This behaviour indicates the presence of a diffusion controlled loss of capacity due to lithium trapping in the aluminium electrode. This is not unexpected since lithium alloys are formed also for aluminium electrodes. It should be pointed out that linear plots of the capacity versus the square root of the time only should be obtained in the presence of semi-infinite planar diffusion.
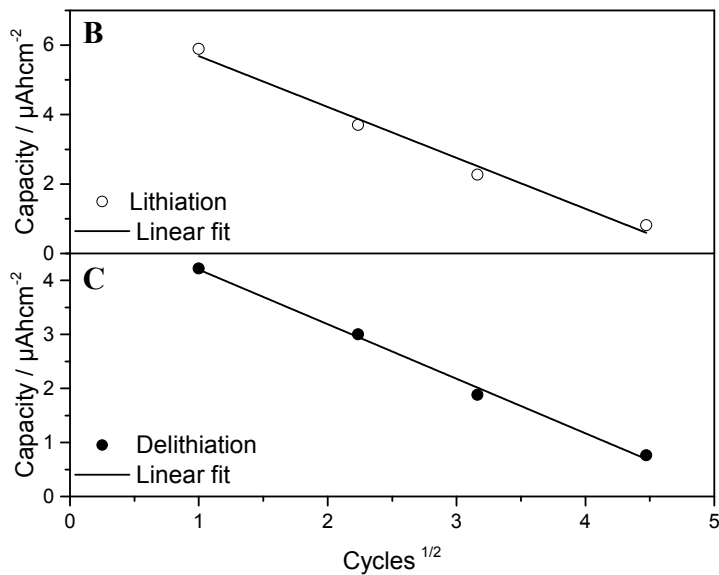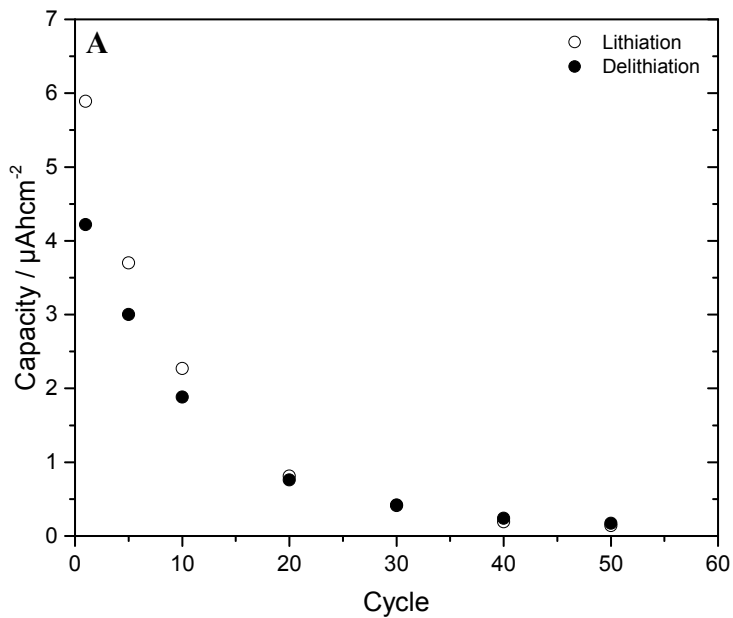
Figure S4. Areal capacity as a function of the cycle number or square root of the cycle number for aluminium nanorod electrodes. (A) Areal capacity versus cycle number plots. **(B and C)** Areal capacity as a function of the square root of the cycle number. The aluminium nanorod electrodes, which had a native Al_2O_3 layer, was cycled between 0.1 and 3.0 V vs. Li^+/Li at a scan rate of 1.0 mV/s. The data were taken from the report by Oltean et al. [5]. The solid lines in (B) and (C) represent linear least squares fits.

5. Capacity losses for Si composite electrodes

As indicated in the main article the capacity loss of 2000 mAh/g during 100 cycles for the Si composite electrode corresponded to an average charge recovery efficiency of about 99% since the capacity left after 100 cycles was about 36% (i.e. $0.99^{100} \approx 0.36$). As this capacity loss of about 20 mAh/g per cycle cannot be explained by SEI formation or volume expansion effects as explained above, the loss should stem from lithium trapping in the silicon electrode. This would indicate the trapping of about 1% of the deposited lithium on each cycle on average. These experiments were carried out with composite electrodes coated on copper or nickel current collectors and the chronopotentiograms for the electrodes can be seen in Figure S5. In analogy with the results for the tin and aluminium nanorod electrodes, linear plots of the capacity as a function of the square root of the time were obtained for the silicon electrodes in the regions where the capacity decrease was seen (see Figure S6). The results for the silicon electrodes containing the copper and nickel current collectors were analogous and a small initial capacity increase was also seen in both cases.

Assuming an initial capacity of 3100 mAh/g, a loss of about 20 mAh/g for an electrode containing 1 mg of silicon would correspond to a loss of about 5 μg of lithium per cycle. Since this is a very small amount it is clear that it would be difficult to detect the trapped lithium after a few cycles unless very sensitive analysis techniques are employed. The total amount of trapped lithium after 100 cycles would, on the other hand, have been about 500 μg. The latter value should be compared to the 920 μg expected for the formation of $Li_{15}Si_4$. The results therefore indicate that the capacity loss was caused by the gradual build-up of the lithium concentration in the silicon electrode (in analogy with the results for the tin nanorod electrodes) and that the average lithium concentration in the silicon electrode after 100 cycles corresponded to about 55% of that expected if $Li_{15}Si_4$ were formed. The trapped amount of lithium, i.e. 500 μg was, incidentally, approximately four times larger than the amount of lithium present in the electrolyte which clearly demonstrates that the trapped amount of lithium must have stemmed from the lithium electrode.

If one (incorrectly) were to assume that the capacity loss was caused by the SEI formation, an SEI layer with a thickness of about 1.2 μm would have to be formed assuming the SEI parameters mentioned above and an electroactive area (including the surface roughness) of 15 cm^2). The weight of this SEI layer (or rather the SEI species formed, as most of them most likely

end up in the electrolyte), would be about 5.6 times larger than the weight of the silicon used in the electrode! It is immediately clear that such SEI effects should have been readily detected when disassembling the cycled cells.
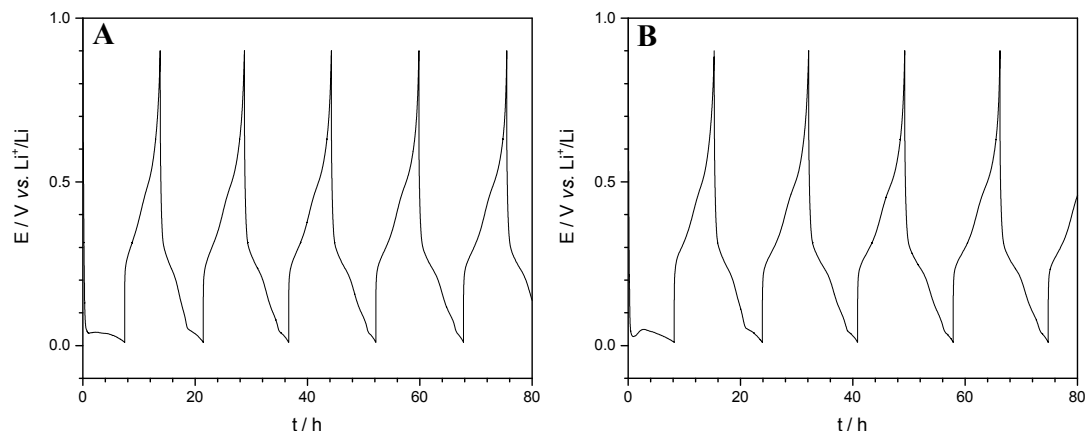
Fig. S5. Chronopotentiograms obtained for the silicon composite electrodes. (**A**) Chronopotentiograms recorded at a rate of C/10 between 0.01 and 0.9 V vs. Li$^+$/Li using a silicon nanoparticle composite electrode cast on a copper current collector and (**B**) Corresponding chronopotentiograms obtained with a nickel current collector.

6. Li trapping affecting the deposition potential

If the lithium concentration in the electrode increases during cycling, a decreasing lithium deposition potential should be observed. This most likely explains the deposition potential changes seen in Figure 1a as well as the differently shaped chronopotentiograms in Figure 1c. In the absence of any overpotentials, a lithium deposition potential of about 0.26 V vs. Li$^+$/Li (see the first cycle in Figure 1a) would correspond to a lithium activity of 10-10 while a potential of about 0.19 V (see the 100th cycle) would suggest a 500 times higher lithium activity at the electrode surface. Note that the lithium surface concentration at the onset of lithium deposition should be much lower than the average lithium concentration in the electrode since lithium oxidation would be the dominating reaction at all potentials higher than the lithium deposition potential. It should also be mentioned that the corresponding variations in the lithium oxidation potential should be small as the lithium surface concentration at the onset of the lithium oxidation should be similar (i.e. high) on all cycles.
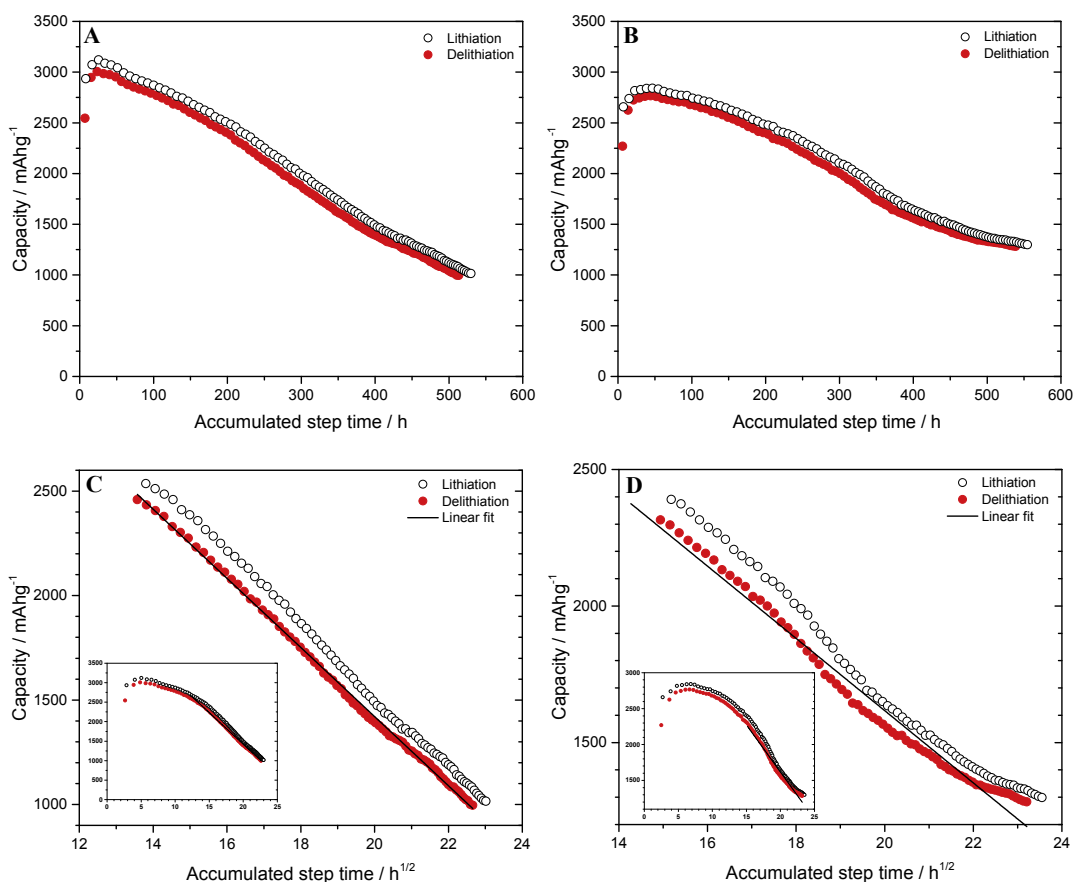
Fig. S6. Specific capacities versus time and square root of time plots for silicon composite electrodes. (**A** and **B**) Specific gravimetric capacities as a function of time. (**C** and **D**) Specific gravimetric capacities as a function of the square root of time. The silicon nanoparticle based composite electrodes were cast on a Ni foil (A and C) and Cu foil (B and D) current collector, respectively. The plots in C and D cover the region between 24 and 100 cycles and 31 to 100 cycles, respectively. The plots for the complete cycle range are presented as insets and the specific gravimetric capacities were calculated using the weights of the silicon nanoparticles. The solid lines in (C) and (D) represent linear least squares fits.

7. Deposition of Li on Si composite electrodes

The amounts of silicon found in the electrodes after the potentiostatic deposition of lithium at 0.1 V vs. Li^+/Li were determined as described in the materials and methods section. It was found that the lithium amounts corresponded to 92% of the total reduction charges, indicating that about 8% of the reduction charge was due to SEI formation. The SEI charge for the electrode exposed to the 200 h reduction time would then correspond to the formation of a 200 nm thick SEI layer. As this is much larger than the thicknesses typically deduced from XPS measurements [9, 11, 13] it is reasonable to assume that most of the SEI species ended up in the electrolyte and that the thickness of the SEI layer was determined by the balance between the SEI formation and

dissolution rates. The SEI formation rate was most likely controlled by the rate of diffusion of the solvent molecules through the SEI layer. It should also be mentioned that the formation of a 10 nm thick SEI layer only would explain 5% of the SEI charge. Based on an assumed steady state SEI thickness of 10 nm, it can be calculated that the SEI dissolution rate was about 1 nm/hour, in good agreement with the value of about 2 nm/hour obtained on the basis of the tin nanorod electrode data. A higher dissolution rate would in fact be expected for the tin nanorod data since these electrodes were continuously reduced and oxidized while the potential was maintained in the SEI formation region throughout the silicon potential step experiments. The data also suggest that there was no significant loss of the SEI due to its oxidation. The partial SEI dissolution phenomenon has in fact been well-documented e.g. as EQCM experiments [12] clearly have shown that only a fraction of the generated species is likely to be present in the SEI layer.

A closer look at the data shows that the initial C/10 chronopotentiometric reduction step gave rise to a reduction charge corresponding to about 70% of that reached after 200 hours of potentiostatic reduction. The deposition charge also increased with the square root of the pulse time (see Figure S7), in agreement with the expected chronocoulometric behaviour, yielding a diffusion coefficient for lithium in the silicon composite electrode of about $1.7 \cdot 10^{-11}$ cm^2/s. A similar value (i.e. $1.3 \cdot 10^{-11}$ cm^2/s) was also obtained based on the data for the initial C/10 lithiation indicating that the diffusion coefficient remained approximately constant throughout the experiment.
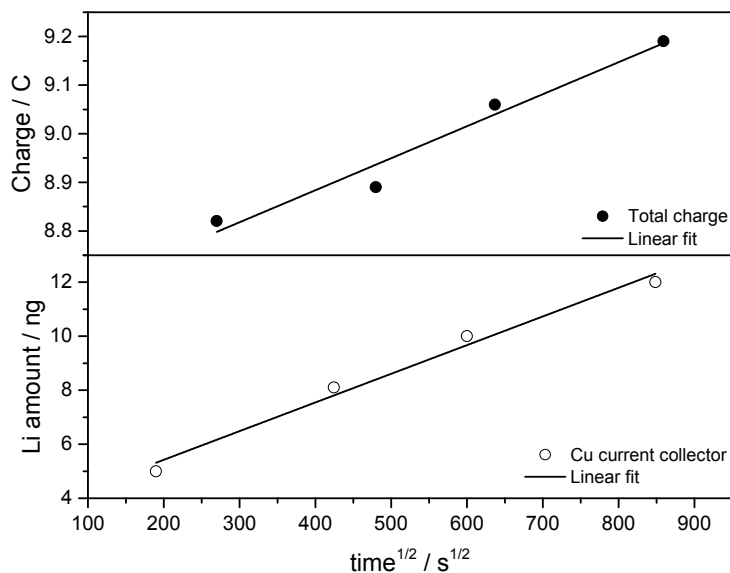
Figure S7. Reduction charge or lithium amount in the copper current collector as a function of the square root of time for a silicon composite electrode. (A) Reduction charge versus the square root of the time for potentiostatic reduction at 0.01 V vs. Li$^+$/Li. **(B)** Amount of lithium found in the copper current collector as a function of the square root of the reduction

time for potentiostatic reduction at 0.01 V vs. Li+/Li. The solid lines represent linear least squares fits.

The total amount of Li found in the silicon electrode after 200 hours of lithium deposition was almost two times larger than the amount present in the electrolyte indicating that the thickness of the Li foil electrode decreased from 50 to about 47 μm during the experiment.

In Figure S7 it can likewise be seen that about 10 ng of lithium was found in the copper current collector after the 200-hour lithium deposition experiment and that there was a linear relationship between the amount of lithium in the copper and the square root of the time indicating a diffusion controlled uptake of lithium. It should, however, be noted that the total amount of lithium found in the silicon electrode after 200 hours was about 600 μg! The loss of lithium due to its diffusion into the copper current collector was hence negligible in this experiment most likely as the thick silicon electrode layer prevented significant amounts of lithium from reaching the copper current collector.

As already indicated, the Li deposition potential should have been determined by the Li activity in the electrode according to the Nernst equation. On the first cycle, this value should have been very low for the pristine tin and silicon electrodes, which means that a deposition potential larger than zero versus Li+/Li should have been obtained in good agreement with the experimental data. On the subsequent cycles the lithium activity in the electrodes should increase due to lithium trapping giving rise to a shift in the lithium deposition potential toward lower potentials. The lithium deposition potential should hence move closer to zero during the cycling. The observed shift cannot be ascribed to an increased iR drop due to a thicker SEI layer as an iR drop effect also should affect the oxidation potentials. It should also be recalled that the SEI formation takes place predominately on the first reduction scan prior to the deposition of lithium. An increasing lithium activity in the electrode would also explain the different shape seen for the chronopotentiograms for the 120th cycle seen in Figure 1C in the main article. On the initial cycle, the lithium activity would be expected to stay almost constant during the reduction due to the diffusion of lithium toward the interior parts of the electrode while a build-up of the surface lithium activity would give rise to a gradual shift in the lithium deposition potential once the surface region becomes saturated with lithium. This explains the difference between the shapes of the chronopotentiograms in Figure 1 in the main article. Similar effects have in fact also been seen for other types of electrode materials [15].

8. Amounts of Li found in Cu, Ni and Ti samples exposed to Li

Table S2 displays the amounts of lithium found in the copper, nickel and titanium samples kept in contact with lithium foils during seven days at 50 °C as determined with ICP-AES. Since μg amounts of lithium were found in all three metals it can be concluded that these metals are unsuitable as current collectors for lithium alloy forming materials and lithium film electrodes.

Table S2. Amounts of lithium found in copper, nickel and titanium samples.

Metal	Area (cm^2)	Li content (µg)	Li content (µg/cm^2)
Cu	1	10.6	10.6
Ni	3.14	8.9	2.8
Ti	1	14.9	14.9

9. Boron-doped diamond lithium diffusion barrier layers

To avoid lithium trapping in the current collector, a high conductivity material which does not readily alloy with lithium and in which the lithium diffusion rate is low should be used. Since the lithium atom is very small, a material with a dense structure is clearly needed. Experiments were therefore performed with films of boron-doped diamond [16] deposited on silicon wafers (see Figures S8 and S9). Pieces of lithium foil were placed on boron-doped diamond samples and the assemblies were sealed into argon filled plastic pouches. The pouches were then stored at 50 °C for up to seven days after which the lithium foil was removed and the lithium contents in the samples were determined. The amount of lithium found in the seven-day sample was about 130 times lower than that found in the corresponding titanium sample and there was also no significant difference between the samples stored for different times (see Figure 4a) indicating that lithium does not readily diffuse into the boron-doped diamond films. The boron-doped diamond films were further tested by exposure to lithium at 20 °C for 12 days after which the lithium foil was removed and the lithium content in the films was determined with TOF-SIMS. No significant amounts of lithium were found in these measurements (see Figure 4d and S11).

Another boron-doped diamond electrode was exposed to five cycles of lithium deposition and oxidation (see below) followed by a 6015 eV HAXPES analysis. The electrode was then removed from the battery cell in its oxidized state (i.e. 1.0 V vs. Li+/Li) and spectra were recorded for the cycled electrode as well as for a pristine boron-doped diamond reference sample. As seen in Figure 4c and S11, no significant differences were found between the spectra for the cycled and pristine boron-doped diamond samples. This supports the hypothesis that the diffusion rate in boron-doped diamond is much lower than those in conventional current collector materials such as copper and nickel.

The performances of cells in which copper and boron-doped diamond thin film based electrodes were exposed to repeated lithium deposition and oxidation were also compared. In these experiments, an initial lithium layer was first deposited on the electrodes using a charge of 1.0 mAh after which the electrodes were cycled using a constant reduction charge of 0.5 mAh, while the lithium oxidation step was subject to a potential window restriction. In Figure S12, it is seen

that the Q_{ox}/Q_{red} ratio generally was lower for the copper electrodes, most likely due to the lithium diffusion problem discussed above. The lower first cycle coulombic efficiency for the boron doped diamond electrode can be explained by a partial loss of the deposited lithium due to the weak interaction between lithium and boron doped diamond and/or a larger SEI formation charge due to the formation of a lithium deposit with a larger surface area. In Figure S13 it is also seen that the overpotential for the lithium deposition on the copper electrode increased significantly during the first 30 cycles while no significant change was seen for the boron-doped diamond electrode. The increased overpotential for the copper electrode is compatible with an increased lithium concentration in the copper electrode. These results demonstrate that boron-doped diamond is a suitable current collector material for lithium alloy and elemental lithium based electrodes.

10. SEM and EDS characterization of boron-doped diamond samples
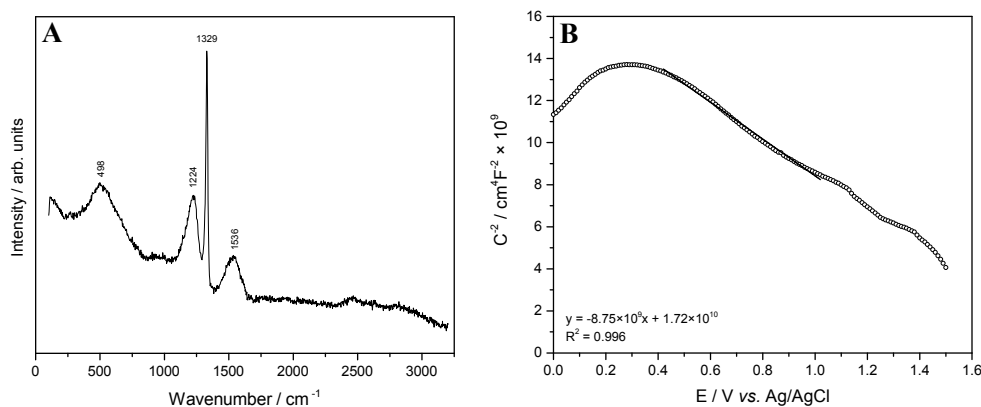
The boron-doped diamond samples were characterized using Scanning Electron Microscopy (SEM) and Energy-Dispersive Spectroscopy (EDS) as shown in Figure S8. It can be seen that the polycrystalline diamond film had a thickness of 4.0 ± 0.1 µm and that the diamond crystals had columnar shape extending outwardly from the surface of the silicon substrate. The EDS results, featuring distribution and relative proportion (i.e. intensity) maps for carbon and silicon, confirm that the sample was composed of a carbon film on top of a silicon substrate.
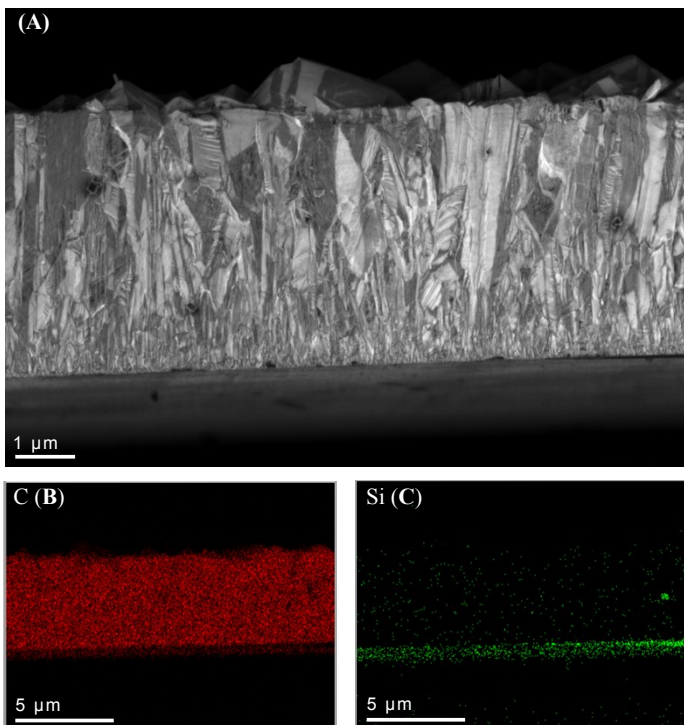
Fig. S8. SEM and EDS characterization of a boron-doped diamond sample. (A) SEM image depicting the cross-section of a boron doped diamond layer deposited on a Si wafer. (B and C) EDS element mappings of the region showing the (B) carbon and (C) silicon distribution in the sample.

## 11. Raman and Mott-Schottky characterization of boron-doped diamond samples

Figure S9 shows a Raman spectrum obtained for a boron-doped diamond sample as well as a Mott-Schottky plot based on three-electrode ac impedance measurements. The Raman spectrum indicates the presence of a characteristic sp3 hybridized diamond peak at 1329 cm^{-1} as well as two broad bands around 500 and 1220 cm^{-1} due to the two phonon density of states maxima for boron-doped diamond. As can be expected for boron-doped diamond, a slight shift to lower wavenumbers by 4 cm^{-1} can be seen primarily for the sp3 hybridization peak. This shift can be ascribed to the Fano-type interference between the discrete zone-centre and continuum of electronic states induced by boron doping. The peak at 1536 cm^{-1} is indicative of the existence of sp2 hybridized carbon atoms on the surface of the sample. A Mott-Schottky plot was employed to estimate the doping level of the boron-doped diamond layer based on the linear region between about 0.4 and 1.0 V vs. Ag/AgCl. The boron concentration in the polycrystalline diamond film was determined using the slope of this linear part employing $N_d = 2/q\varepsilon\varepsilon_0$ (slope)$^{-1}$ where q is the electronic charge, ε is the dielectric constant for diamond, and ε_0 denotes the relative permittivity of free space. Based on the linear curve fit $y = -8.75 \cdot 10^9 x + 1.72 \cdot 10^{10}$, a boron concentration, i.e. N_d, of $2.93 \cdot 10^{21}$ atoms/cm^3 was obtained. The flat band potential (E_{fb}) was also found to be 1.966 V (based on the intersection of the linear line with the potential axis). Using the boron doping level mentioned above, the conductivity of this sample was estimated to be approximately 1000 S/cm, which was sufficiently to allow the boron-doped diamond samples to be used as electrodes.

Figure. S9. Raman and Mott-Schottky characterization of the boron-doped diamond films. (A) Raman spectra featuring the characteristic sp3-hybridised diamond structure. (B) Mott-Schottky plot used to estimate the doping level of the obtained boron-doped diamond film.

12. TOF-SIMS characterization of a boron-doped diamond sample exposed to Li

The results of a TOF-SIMS analysis of a boron-doped diamond sample kept in contact with a lithium foil at 20 °C for 12 days are depicted in Figure S10. It can be seen that no significant amounts of lithium could be found independent of whether the boron-doped diamond layer was partially or fully penetrated during the sputtering process. Since the lithium intensities were lower than those for potassium in both cases it is reasonable to assume that the lithium intensities stemmed from traces of lithium in the samples. It should also be noted that the TOF-SIMS sensitivity for lithium should be high.
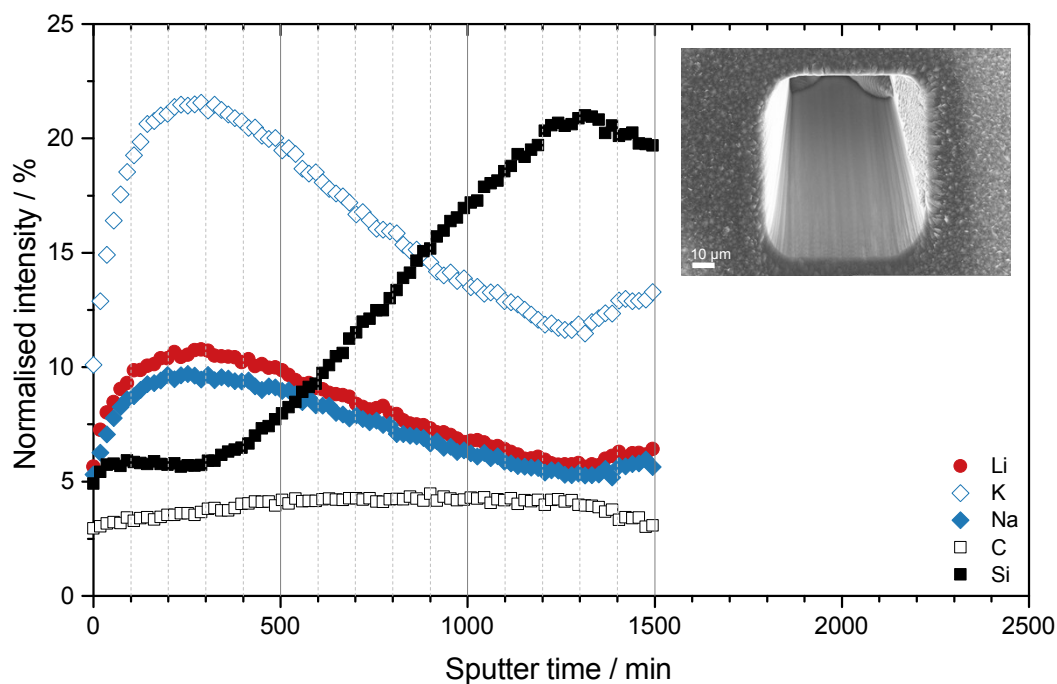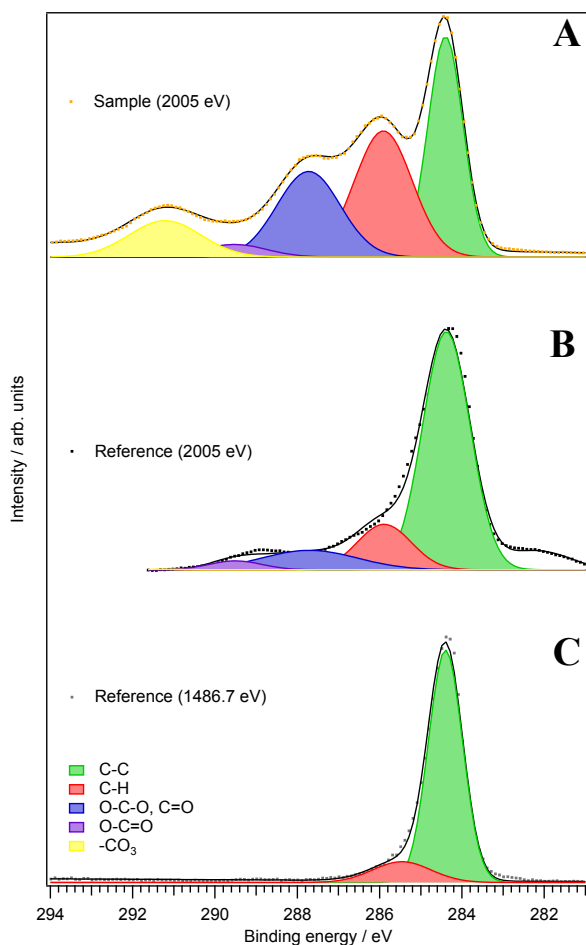

Fig. S10. TOF-SIMS analyses of a boron-doped diamond electrode exposed to lithium at room temperature for 12 days. (A) Sputter profile not penetrating the boron-doped diamond film and (B) Sputter profile reaching the silicon substrate underneath. The insets show SEM images of the surfaces after the TOF-SIMS analyses where the scale bars represent 10 μm.

13. HAXPES experiments on a cycled boron-doped diamond electrode

A boron-doped diamond electrode was exposed to five cycles of lithium deposition and oxidation followed by an HAXPES analysis with an energy of 6015 eV. The studied boron-doped diamond electrode was removed from the battery cell in its oxidized state (i.e. 1.0 V vs. Li^+/Li) and spectra were recorded for the cycled boron-doped diamond electrode as well as for a pristine boron-doped diamond reference sample as seen in Figure 4c in the main article. Since HAXPES allows studies at a deeper depth than conventional XPS this technique should enable

the detection of lithium present in the boron-doped diamond electrode without having to sputter the electrode surface. Lithium redeposition can be a significant problem during the recording of sputter profiles for samples coated with a lithium ion containing SEI layer. No significant differences were found between the C1s spectra for the cycled and pristine boron-doped diamond samples as a single peak due to sp3 hybridized C-C bonds was found at 284.5 eV in both spectra. Since there was no evidence of any surface species it is also clear that mainly the bulk of the samples was studied. Spectra collected with an energy of 2005 eV did, however, indicate the presence of ether, C-H and $C-CO_3$ peaks which all are characteristic features of the SEI layer present on the surface of the cycled electrode. Only C-C and C-H peaks were observed for the uncycled electrode as is seen in Figure S11. The small peak observed at 282 eV was found to be an instrumental induced auger peak as no such feature could be observed by in-house XPS. Since it is reasonable to assume that the presence of any lithium in the boron-doped diamond sample should affect the C-C binding energy these results support the hypothesis that the rate of lithium diffusion in boron-doped diamond is low and that boron-doped diamond therefore could be used as lithium diffusion barrier layers as well as current collectors for lithium alloy and elemental lithium based electrode materials.

Fig. S11. HAXPES surface analyses of boron-doped diamond electrodes. (A) HAXPES C1s spectra obtained with an energy of 2005 eV for a boron-doped diamond electrode cycled versus a lithium counter electrode as well as (B) for an uncycled boron doped diamond electrode with an energy of 2005 eV and (C) 1486.7 eV.

14. Li deposition on a boron doped diamond film electrode

Deposition and oxidation of lithium on boron-doped diamond electrodes were studied in a chronopotentiometric experiment in which lithium was first deposited on the electrodes using a charge of 1.0 mAh. The electrodes were then cycled using a fixed reduction (i.e. deposition) charge of 0.5 mAh while the oxidation (i.e. stripping) step was subject to a potential window restriction. In the chronopotentiograms depicting the first 30 cycles shown in Figure S12 it can be seen that the potential required for the deposition of lithium on the copper electrode increased continuously during the cycling. The results for the copper electrode indicate that the surface concentration of lithium concentration in the copper electrode increased during the cycling. The change in the shape of the curves after 28 cycles for the copper electrode can be ascribed to a short circuiting of the cell as a result of dendrite formation. For the boron-doped diamond electrode there was, on the other hand, no significant change in the cycling behaviour indicating that there was no lithium diffusion problem with this electrode.
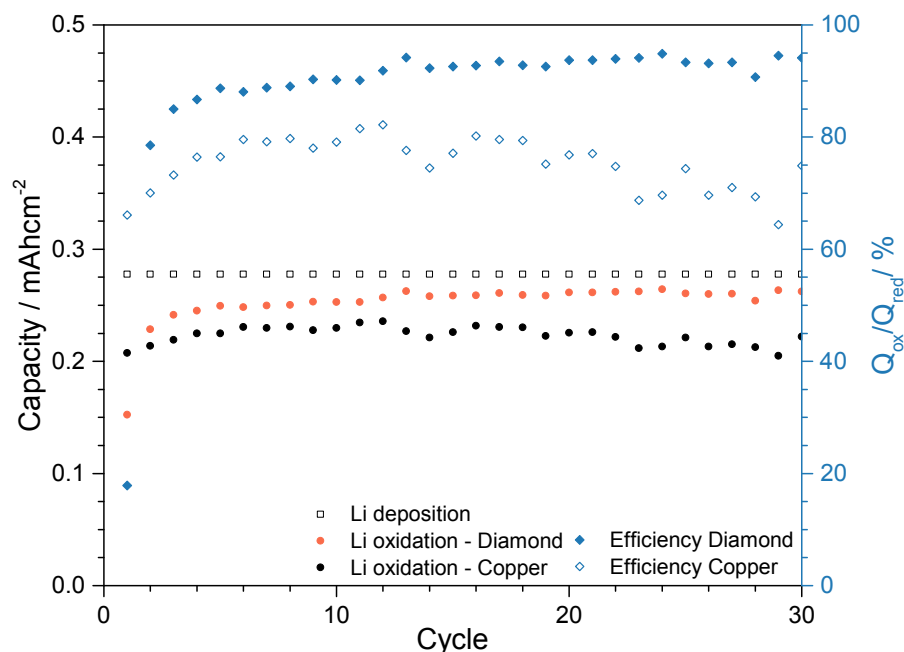
Fig. S12. Reversible Li deposition/dissolution on boron-doped diamond and copper electrodes. Lithium deposition and oxidation charges as well as Q_{ox}/Q_{red} ratios as a function of the cycle number for boron-doped diamond and copper, respectively.
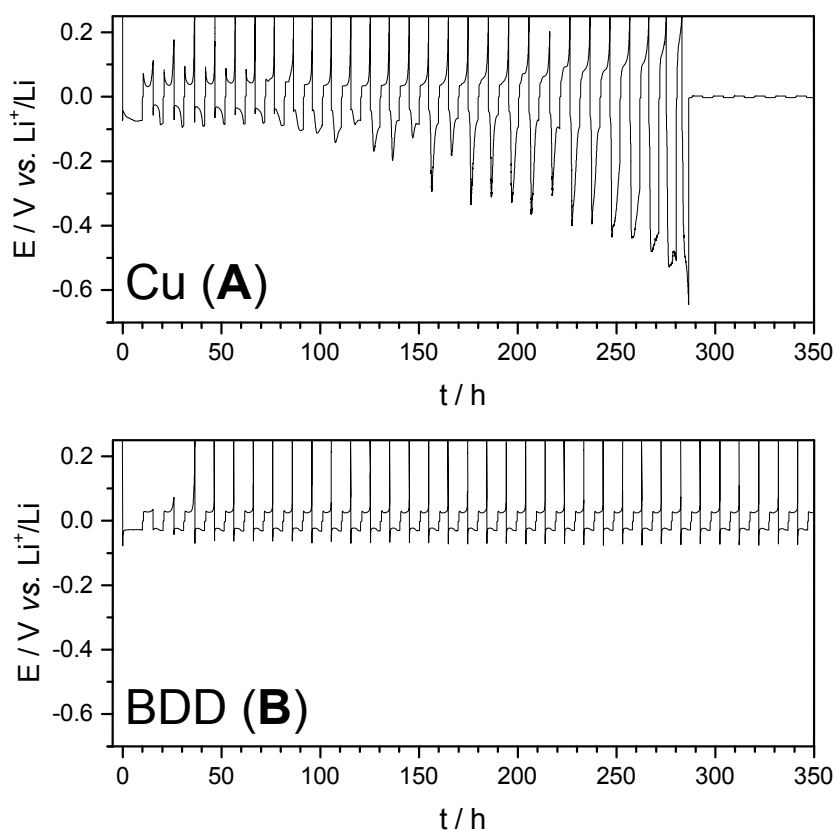
Fig. S13. Chronopotentiograms for the deposition and oxidation of lithium on a copper and a boron-doped diamond electrode, respectively. (A) Lithium deposition and oxidation on a copper electrode. (B) Lithium deposition and oxidation on a boron-doped diamond electrode. The first 30 cycles are shown in both figures.

References

1.   M. Valvo, D. Rehnlund, U. Lafont, M. Hahlin, K. Edström and L. Nyholm, *Journal of Materials Chemistry A*, 2014, **2**, 9574-9586.
2.   G. Oltean, L. Nyholm and K. Edström, *Electrochimica Acta*, 2011, **56**, 3203-3208.
3.   S. Böhme, K. Edström and L. Nyholm, *Electrochimica Acta*, 2015, **179**, 482-494.
4.   M. N. Obrovac and V. L. Chevrier, *Chemical Reviews*, 2014, **114**, 11444-11502.
5.   G. Oltean, C-W. Tai, K. Edström and L. Nyholm, *Journal of Power Sources*, 2014, **269**, 266-273.
6.   K. Nishio, T. Yanagishita, M. Yoshida, T. Hayakawa and H. Masuda, *Electrochemistry Communications*, 2015, **59**, 13-15.
7.   K. Ui, K. Yamamoto, K. Ishikawa, T. Minami, K. Takeuchi, M. Itagaki, K. Watanabe and N. Koura, *Journal of Power Sources*, 2008, **183**, 347-350.

8.   S. Leroy, F. Blanchard, R. Dedryvère, H. Martinez, B. Carré, D. Lemordant and D. Gonbeau, *Surface and Interface Analysis*, 2005, **37**, 773-781.

9.   K. C. Högström, S. Malmgren, M. Hahlin, M. Gorgoi, L. Nyholm, H. Rensmo and K. Edström., *Electrochimica Acta*, 2014, **138**, 430-436.

10.   I. Yoon, D. P. Abraham, B. L. Lucht, A. F. Bower and P. R. Guduru, *Advanced Energy Materials*, 2016, **6**, 1600099.

11.   K. Edström, M. Herstedt and D. P. Abraham, *Journal of Power Sources*, 2006, **153**, 380-384.

12.   D. Aurbach, M. Moshkovich, Y. Cohen and A. Schecter, *Langmuir*, 1999, **15**, 2947-2960.

13.   A. Meitav and E. Peled, *Journal of Electroanalytical Chemistry*, 1982, **134**, 49-63.

14.   D. Rehnlund, M. Valvo, C-W. Tai, J. Ångström, M. Sahlberg, K. Edström and L. Nyholm, *Nanoscale*, 2015, **7**, 13591-13604.

15.   W. Wei, F. Björefors and L. Nyholm, *Electrochimica Acta*, 2015, **176**, 1393-1402.

16.   R. Kalish, *Journal of Physics D: Applied Physics*, 2007, **40**, 6467-6478.